Journal of Power Sources 196 (2011) 8553–8560

Contents lists available at ScienceDirect

Journal of Power Sources

journal homepage: www.elsevier.com/locate/jpowsour

Catalytic activity of cobalt on nanotextured polymer films for hydrogen production

Niranjan A. Malvadkar[a,b], Koray Sekeroglu[a], Walter J. Dressick[c], Melik C. Demirel[a,d,*]

[a] Department of Engineering Science, and Materials Research Institute, Pennsylvania State University, University Park, PA 16802, United States
[b] Core Research and Development, Dow Chemical Company, Midland, MI 48674, United States
[c] Naval Research Laboratory, Code 6910, 4555 Overlook Avenue, S.W., Washington, DC 20375, United States
[d] Wyss Institute for Bioinspired Engineering, Harvard, Cambridge, MA 02138, United States

ARTICLE INFO

Article history:
Received 21 March 2011
Received in revised form 25 May 2011
Accepted 26 May 2011
Available online 2 June 2011

Keywords:
Cobalt
Catalyst
Hydrogen generation
Borohydride
Polymer
Poly(*p*-xylylene)

ABSTRACT

We describe the mechanism of cobalt and ligand binding on nanotextured poly(chloro-*p*-xylylene) (PPX) films as supports for catalytic release of H_2 from alkaline aqueous solutions of sodium borohydride. Cobalt catalysts are prepared on nanotextured PPX substrates via electroless plating using a Sn-free Pd(II) colloid with adsorbed pyridine ligand as an adhesion promoter. Gas physisorption studies on PPX, using N_2 and CO_2 as probe gases, indicate the presence of micropores (~1 to 2 nm width) responsible for the adsorption and non-covalent stabilization of pyridine molecules on the nanotextured surface. The strongly adsorbed pyridine molecules promote Co adhesion onto the PPX surface during subsequent electroless deposition, thereby retaining the metal's catalytic activity for H_2 evolution even after multiple reaction cycles. In contrast, conventionally deposited PPX is devoid of any nanotexture and contains fewer micropores capable of stabilizing pyridine adsorption, resulting in poor metallization and catalytic activity for H_2 evolution. We also demonstrate the effect of patterning the PPX substrate as a means to further improve the activity of the Co catalyst to achieve H_2 evolution rates comparable to those obtained using precious metal catalysts.

© 2011 Elsevier B.V. All rights reserved.

1. Introduction

The development of sustainable, environment-friendly, and low-cost energy sources is undoubtedly the greatest challenge of the 21st century. Despite the soaring prices of hydrocarbon fuels, alternative energy technologies of today remain prohibitively expensive for a complete replacement of existing fossil-fuel technologies. Fortunately, the development of nanoscale interface technologies in the past two decades has brought fascinating breakthroughs in alternative energy technologies, notably in photovoltaics, batteries and fuel cells. Hydrogen fuel cells, in particular, are now on the verge of commercialization in transportation applications, albeit with certain unresolved issues. One of the critical challenges, particularly for mobile applications, is the cost-effective extraction and safe storage of hydrogen. Metal hydrides have been envisaged as the potential candidates for hydrogen storage in mobile applications due to their favorable hydrogen storage capacities and their abilities to release hydrogen via thermal activation or hydrolysis, making them a safer alternative to compressed or liquefied hydrogen [1,2].

Among various metal hydrides that have been studied, sodium borohydride ($NaBH_4$) is a very attractive choice for hydrogen storage in mobile applications. $NaBH_4$ has 10.9 wt.% hydrogen content and can form a stable aqueous solution at high pH (>9), allowing safe transportation without any hydrogen release. Hydrogen can be rapidly extracted from $NaBH_4$ solution by means of a metal catalyst (i.e., Pt [3] or Ru [4]). The reaction, in theory, produces up to eight hydrogen atoms (four molecules) from four atoms of hydrogen in the $NaBH_4$ and water each according to Eq. (1):

$$NaBH_4 + 2H_2O \xrightarrow{\text{catalyst}} NaBO_{2(s)} + 4H_{2(g)} \quad (1)$$

Furthermore, the catalytic hydrolysis of $NaBH_4$ is exothermic ($\Delta H = -217\ kJ\ mol^{-1}$) [5] and hydrogen can therefore be extracted at room temperature without any input heat. Moreover, due to the absence of any side-reactions, the hydrogen obtained is very pure and the byproduct of the hydrolysis reaction (i.e., $NaBO_2$) is environmentally benign and can be recycled back to $NaBH_4$, e.g., by reaction with MgH_2 [6] or methane [7] or via various electrochemical pathways [8]. However, economical viability of the $NaBH_4$-based hydrogen storage systems depends on the development of: (i) cheaper alternatives for the present noble-metal

* Corresponding author at: Department of Engineering Science, and Materials Research Institute, Pennsylvania State University, University Park, PA 16802, United States. Tel.: +1 8148632270; fax: +1 8148659974.
E-mail address: mdemirel@engr.psu.edu (M.C. Demirel).

0378-7753/$ – see front matter © 2011 Elsevier B.V. All rights reserved.
doi:10.1016/j.jpowsour.2011.05.071

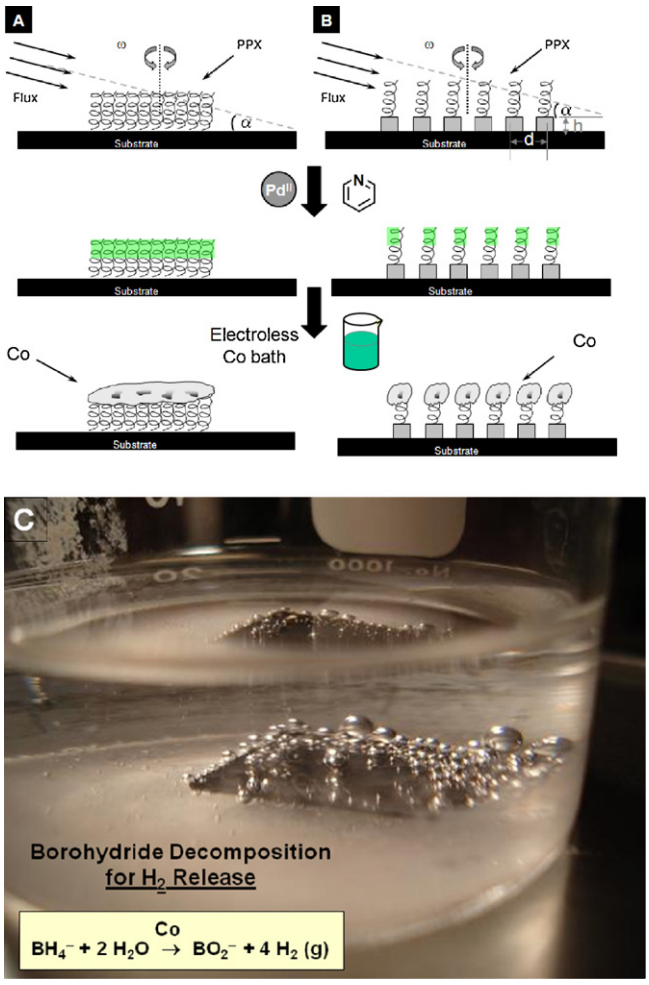

Fig. 1. Schematic of growth of catalytic Co film on (A) nanoPPX and (B) patterned nanoPPX via the noncovalent electroless metallization technique. (C) The optical picture of the catalytic Co-nanoPPX substrate in $NaBH_4$ solution.

catalysts without compromising the hydrogen discharge kinetics, and (ii) a low-cost $NaBH_4$ production method.

Recently, we proposed a novel electroless route to prepare a Co metal-based H_2 catalyst [9] supported on nanotextured poly(chloro-*p*-xylylene) (PPX) (hereafter referred to as nanoPPX). The hydrogen discharge rate from $NaBH_4$ decomposition using the Co catalyst (~4250 mL g^{-1} min^{-1}) is similar to that obtained on some of the prominent Ru-based [5,11] catalysts (~4000 to 24,000 mL g^{-1} min^{-1}) reported in the literature. The nanoPPX films are readily prepared via a one-step, bottom-up vapor deposition approach called oblique angle polymerization (OAP) by inducing angular constraint to the *p*-cyclophane monomer vapor flux during surface polymerization [10]. Fig. 1A and B depicts a schematic for the preparation of the Co catalyst on the non-patterned and patterned nanoPPX films, respectively. Conformal Co metallization over the nanoPPX is initiated by means of an aromatic ligand (e.g., pyridine), which is first physisorbed into the parylene polymer comprising the nanoPPX film [12], followed by treatment with a Pd^{II}-based colloidal dispersion for initiating the electroless Co metal deposition reaction. The first step of depositing metal films, i.e., non-covalent immobilization of ligand molecules, allows functionalization of nanoPPX surface without modifying the parylene film chemistry or morphology. Non-covalent functionalization is a critical step in determining the morphology of the Co metal layer and therefore influencing its catalytic properties. Despite the presence of non-covalent interactions, metal or ceramic particles deposited via this route are surprisingly stable and readily pass the Scotch® tape adhesion test [12,13]. While functionalization of the nanoPPX film results in deposition of a continuous and conformal metal layer, analogous plating procedures on a conventionally deposited "planar" (i.e., devoid of any nano-morphological features) PPX film leads to a non-continuous and patchy metal layer [9,13]. Further investigation revealed that efficient immobilization of aromatic ligand molecules is facilitated by the formation of $\pi-\pi$ interactions with aromatic moieties in the backbone chains within the amorphous regimes that dominate the nanoPPX structure. In contrast, the more compact (i.e., crystalline) arrangement of PPX chains in a planar PPX structure cannot readily incorporate ligand molecules due to steric effects, resulting in insufficient functionalization for metal growth.

The study presented herein is aimed at developing a model of metal growth on the nanoPPX catalyst support substrate and further understanding the mechanism of pyridine adsorption in the nanoPPX films. The nanoPPX offer the opportunity to precisely control the morphology and topography of the surface, and therefore also the bound Co metal, with reasonable precision. Specifically, we studied N_2 and CO_2 sorption to comparatively evaluate the surface area and microporosity of planar PPX and nanoPPX films. We quantified the pyridine adsorption using the quartz crystal microbalance (QCM) technique. Hydrogen release rates were measured on catalytic Co films grown on nanoPPX supports with varying microporosity, achieved by means of annealing the nanoPPX at different temperatures while retaining the nanohelix morphology. A comprehensive metal growth model encompassing the present and previous [12,13] results is proposed. Finally, we patterned PPX substrates as a means to increase the catalyst surface area, thereby enhancing the hydrogen release (Fig. 1C).

2. Results and discussion

We present three different adsorption studies to elucidate the difference in pyridine adsorption rate and to contrast the pore structures for planar PPX versus nanoPPX films.

2.1. Sauerbrey's method

The first method employed utilizes the quartz crystal microbalance (QCM) to assess pyridine adsorption by planar and nanoPPX films deposited onto quartz crystal substrates. For the QCM technique, the surface density (ρ_s) of the adsorbate is linearly proportional to the change in the resonance frequency, as represented by the Sauerbrey's equation [14]

$$\Delta f_s^{\text{mass}} = -\left(\frac{2f_s^2}{\sqrt{\bar{c}_{66}\rho_Q}}\right) \times \rho_s \tag{2}$$

where f_s, $\bar{c}_{66}$ and ρ_Q are the first-harmonic resonance frequency, piezoelectric constant and density of the quartz crystal, respectively. Fig. 2 shows the vapor phase pyridine adsorption isotherms of planar and nanoPPX films normalized with their respective BET [15] surface areas (obtained from N_2 adsorption isotherm data, see Supplementary Material Fig. S-1). The pyridine adsorption isotherm of a nanoPPX film shows three distinct segments, while that of a planar PPX film exhibits a continuous monotonic increase of pyridine coverage. The initial segment (<~250 mM pyridine) of the adsorption isotherm of a nanoPPX film is nearly linear and coincides with the isotherm of a planar PPX film, implying adsorption on the surface. At ≈250 mM pyridine, a steep increase in pyridine adsorption is observed in the nanoPPX film, which can be attributed to the condensation of pyridine in the porous structures of nanoPPX [16]. In contrast, this is not observed for planar PPX film due to the lack of such pores for pyridine condensation. The final segment

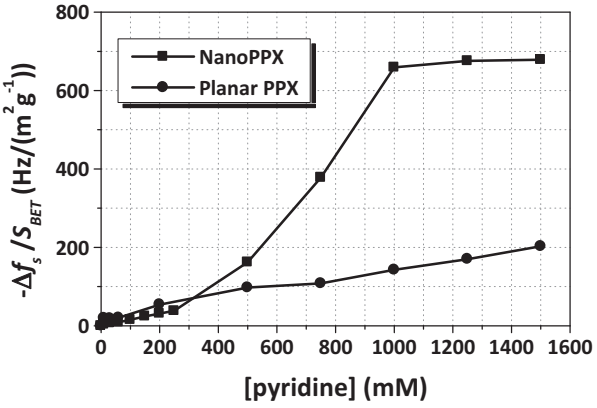

Fig. 2. Vapor phase pyridine adsorption isotherm on nanoPPX and planar PPX films. The frequency change, Δf_s, was normalized with the BET surface area, S_{BET}, of the two films.

(>∼1 M pyridine) of the adsorption isotherm on the nanoPPX film is nearly horizontal as a result of the build-up of pyridine molecules on the outermost surface of the film culminating in adsorption saturation. The saturated Δf_s is equivalent to 0.46 cm^3 g^{-1} of pyridine in the nanoPPX film obtained by applying the Sauerbrey's equation (Eq. (2)) [14]. The contrasting features of the pyridine adsorption isotherms of the two films stem from the difference in their pore structures, resulting in the observed difference in the metallization behavior and catalytic activity [9,12]. In order to further understand the difference in the pore structures of the two PPX morphologies, we present detailed N_2 and CO_2 sorption studies using the Barret–Joyner–Halenda (BJH) and Dubinin–Astakhov (DA) methods.

2.2. Barret–Joyner–Halenda (BJH) method

Results for determination of the mesopore size distribution using the BJH method [17] are illustrated in Fig. 3. Results are derived from Fig. S-1 via application of the Kelvin equation, which is given by $\ln(p/p_0) = 2\gamma V_m/rRT$, where γ is the condensate surface tension, V_m is the molar volume of the condensate, and r is the radius of the droplet. A planar PPX film exhibits a cumulative mesopore volume of 2.0×10^{-4} cm^3 g^{-1}, while a nanoPPX film, on the other hand, shows a broad size distribution of mesopores centered at ∼35 nm resulting in a cumulative mesopore volume of 4.76×10^{-2} cm^3 g^{-1}. The mesopores in a nanoPPX film comprise the inter-nanohelix spacing created by the aligned nanohelix morphology and are responsible for the observed hysteresis due to capillary condensation at normalized pressure, $p/p_0 \sim 0.85$ in the

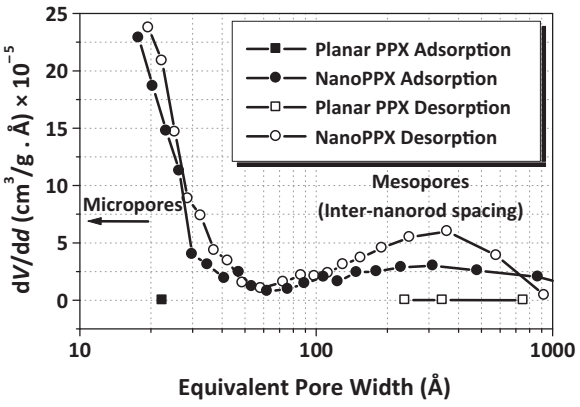

Fig. 3. Differential pore volume distribution obtained from BJH method using N_2 isotherm data on planar and nanoPPX films at 77.35 K.

N_2 isotherm (Fig. S-1). In addition, the mesopore size distribution shows a steep increase near the micropore regime (∼3 nm) signifying the presence of micropores in a nanoPPX film not observed for the planar PPX film. However, due to the inapplicability of the Kelvin equation in the micropore regime, pore size distribution for sizes less than 2 nm cannot be calculated using the BJH method. Therefore, it is necessary to use a CO_2 adsorption isotherm to evaluate the microporosity in the nanoPPX film.

We measured CO_2 adsorption at 273 K in the range $0.00 \le p/p_0 \le 0.01$ (corresponding to p = 0–266 torr) on four films: pristine nanoPPX, pristine planar PPX, nanoPPX film functionalized with aqueous pyridine and nanoPPX film functionalized with vapor pyridine (each for 48 h). Two of these four films, namely pristine planar and nanoPPX film functionalized with vapor pyridine did not show any CO_2 adsorption. This behavior is consistent with a lack of micropore structures for the pristine planar PPX film and a lack of *accessible* micropores due to the presence of strongly adsorbed pyridine vapor for the nanoPPX film, as suggested by the QCM results shown in Fig. 2.

In contrast, CO_2 adsorption isotherms are observed for pristine nanoPPX and pyridine(aq)-functionalized nanoPPX films, as shown in Fig. S-2 (Supplementary Information). CO_2 adsorption in a pristine nanoPPX film is clearly higher compared to that in pyridine(aq)-functionalized nanoPPX, indicating the presence of a larger cumulative micropore volume in a pristine film. These results are consistent with earlier observations concerning electroless metallization of nanoPPX films treated with pyridine (aq) solutions [12]. Specifically, pyridine (aq) solutions do not penetrate the interstitial regions between the PPX nanohelices to the same extent as pyridine vapor due to the hydrophobic nature of the parylene surface [18,19]. Therefore, pyridine adsorption and subsequent metal deposition are limited to the outer portions of each nanohelix, as demonstrated by cross-sectional scanning electron microscopy images the nanoPPX films after metal plating [9,13,20,21]. Consequently, micropores accessible to CO_2 remain for those portions of each nanohelix not contacted by the pyridine (aq) solution, consistent with our observation of a CO_2 adsorption isotherm having a lower cumulative micropore volume for the pyridine (aq) treated nanoPPX films in Fig. S-2.

2.3. Dubinin–Astakhov (DA) method

Cumulative surface area and pore volume data obtained from the N_2 isotherms (Supplementary Material, Fig. S-1) of planar and nanoPPX films are summarized in Table 1. In order to calculate the cumulative micropore volume in the nanoPPX film, the DA model [22] was applied to the CO_2 adsorption data. Mathematically, the DA model can be expressed as:

$$\ln\ Q = \ln\ Q_0 - \left[\left(\frac{RT}{\beta E_0}\right)\ln\left(\frac{p_0}{p}\right)\right] \quad (3)$$

where Q_0 is the limiting micropore volume, E_0 is the characteristic adsorption potential, n is the empirically determined exponent, and β represents the affinity coefficient for the adsorbate. In the above equation, Q represents the volume of adsorbate (i.e., CO_2) adsorbed in the micropores at adsorption potential A. The adsorption potential, A, is dependent on the temperature, T, and relative pressure of the adsorbate (p/p_0) and is given by:

$$A = -\Delta G = -RT\ln\left(\frac{p}{p_0}\right) \quad (4)$$

The y-intercept of the DA model (Eq. (3)) yields the limiting micropore volume while the characteristic adsorption potential can be obtained from the slope of the linear curve.

The linearized DA plots for pristine and pyridine(aq)-functionalized nanoPPX films are shown in Fig. S-3 (Supplementary

Table 1
Surface area and porosity data from N_2 and CO_2 adsorption isotherm.

	BET surface area (S_{BET}, $m^2\ g^{-1}$)[a]	BJH total mesopore volume ($cm^3\ g^{-1}$)[a]	Micropore limiting volume (Q_0, $cm^3\ g^{-1}$)[b]	Micropore limiting area ($m^2\ g^{-1}$)[b]
Pristine planar PPX	3.1574	0.0002	–[c]	–[c]
Pristine NanoPPX	12.6835	0.0476	0.433	1129.7
PYR(aq)-NanoPPX	–	–	0.021	51.503
PYR(vap)-NanoPPX	–	–	–[c]	–[c]

[a] Calculated from the adsorption branch of the N_2 isotherm (Supplementary Information, Fig. S-1).
[b] Obtained by applying Dubinin–Astakhov equation (Eq. (3)) on CO_2 adsorption isotherm.
[c] No adsorption data could be obtained from these samples, i.e., no CO_2 adsorption occurs.

Material). As expected, the pristine nanoPPX film exhibits a higher Q_0 value compared to a pyridine(aq)-functionalized nanoPPX film (Table 1) due to the occupation of a fraction of the micropores by pyridine in a pyridine(aq)-functionalized nanoPPX film. The limiting micropore volume of a pristine nanoPPX film (0.433 $cm^3\ g^{-1}$) is close to the pyridine condensate volume (0.46 $cm^3\ g^{-1}$) and an order of magnitude higher compared to the cumulative BJH mesopore volume (0.0476 $cm^3\ g^{-1}$, Table 1), which confirms that pyridine adsorption proceeds via the micropore filling mechanism.

The differential pore size distribution from the CO_2 adsorption data on the two films is obtained by solving the inverse Stoeckli integral equation [23]

$$\Theta(p) = \int f(x)\theta(p,x)dx \quad (5)$$

where $\Theta(p)$ is the experimental "global" isotherm, $f(x)$ is the micropore size distribution function, and $\theta(p, x)$ is the "local" isotherm given by the DA equation (Eq. (3)). In this work, an *a priori* distribution function, $f(x)$, with a Gaussian distribution is considered. Finally, the micropore size distribution obtained by iteratively solving the inverse integral equation (Eq. (5)) is shown in Fig. 4. The differential pore size distribution obtained from CO_2 adsorption data juxtaposes well with that obtained from the BJH model (Fig. 3), verifying the accuracy of the two methods. From the above data, we conclude that the structure of a nanoPPX film is dominated by micropores of ~1 to 2 nm width, which are sites where pyridine adsorption occurs.

2.4. The effect of annealing on the catalytic behavior

Annealing of the nanoPPX film decreases the surface disorder, which is evident by the increase in the peak magnitude of the Bragg reflections in the X-ray diffraction (XRD) pattern (Supplementary Information, Fig. S-4). After subjecting the as-deposited and annealed nanoPPX films of Fig. S-4 to pyridine (aq) treatments for 48 h and Co metallizations for 60 min, the resulting composite films were tested as catalysts for hydrogen evolution in $NaBH_4$ (aq) solution. Hydrogen release rates are plotted against the annealing temperatures in Fig. 5. The hydrogen release rate remains essentially unchanged until an annealing temperature of 170 °C (443 K) and drops drastically at 220 °C (493 K).

The hydrogen release rates summarized in Fig. 5 can be directly correlated with changes in the levels of micropores containing strongly bound pyridine ligand in the annealed films. Relative pyridine adsorption strengths were measured using a QCM that permits simultaneous monitoring of both resonance frequency (f_s) and resistance (R). In this case, the measured Δf_s term arises from two components [24]. The first component represents the contribution from strongly adsorbed pyridine in the micropores on the nanoPPX surface. This pyridine can be considered as a rigid mass bound to the nanoPPX surface and resonating in unison with it. The second contribution is a viscous component to the frequency shift due to contact of the surface with a Newtonian liquid (*cf.* pyridine solution).

Fig. 6A shows frequency shifts (Δf_s) for annealed and as-deposited nanoPPX samples submerged step-by-step in aqueous solutions containing progressively higher pyridine concentrations. These plots of Δf_s versus pyridine concentration each exhibit an abrupt increase in response at a certain pyridine level, illustrating adsorption by the pore-filling mechanism. Furthermore, the point at which an abrupt increase in Δf_s occurs varies with the annealing temperature. For instance, the as-deposited nanoPPX sample exhibits the abrupt increase in Δf_s at ≈495 mM pyridine, while a similar increase in Δf_s occurs at ≈350 mM pyridine for a nanoPPX sample annealed at 493 K. The concentration (or relative pressure) at which such an inflection point occurs is a relative measure of the size of the micropores; an inflection point at lower concentration (or relative pressure) values indicates smaller micropore size, and vice versa [25]. At the same time, the ΔR versus pyridine concentration plots shown in Fig. 6B, which illustrate the dissipation loss of the QCM vibration arising from the liquid contact, clearly indicate higher dissipation losses for annealed samples, signify-

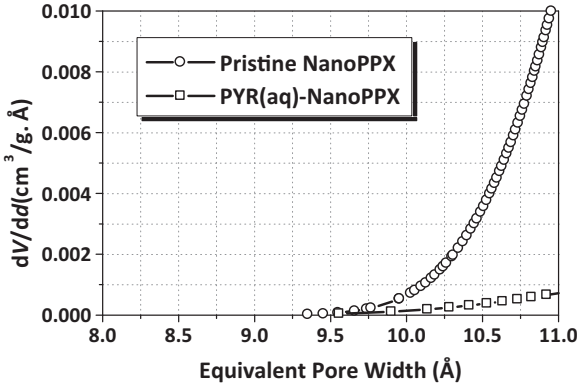

Fig. 4. Differential pore volume distribution obtained from CO_2 adsorption data on pristine and pyridine (aq)-functionalized nanoPPX.

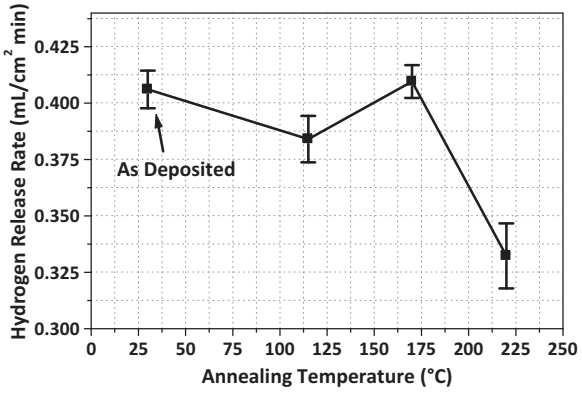

Fig. 5. Effect of nanoPPX annealing on hydrogen release rate of Co/nanoPPX catalysts.

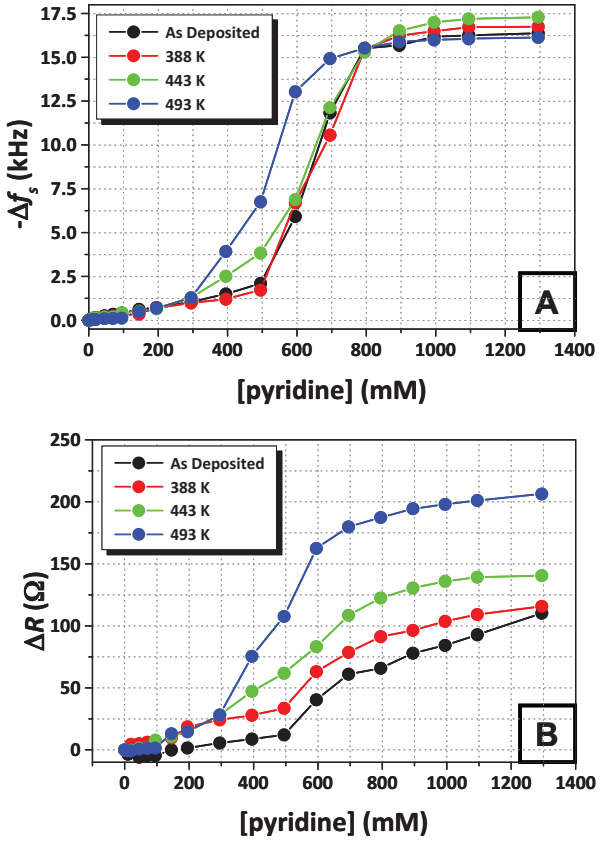

Fig. 6. Plot of (A) equilibrium frequency shifts (Δf_s) and (B) equivalent resistance change (ΔR) against pyridine (aq) concentration. Three films were annealed at 388, 443, and 493 K prior to QCM experiments.

ing the presence of weakly bound pyridine or pyridine build-up on the external surface. These behaviors, taken together, are consistent with a mechanism in which the higher crystallinity induced by annealing leads to a decrease in nanoPPX film microporosity.

Plots of Δf_s versus ΔR for all samples in Fig. 7 allow a clear distinction between the contribution from rigidly adsorbed pyridine (i.e., pyridine filled micropores) and weakly bound pyridine. For an as-deposited nanoPPX sample, the progressively higher slope in the $\Delta f_s - \Delta R$ plot until $\Delta R \approx 62\,\Omega$ confirms the increase in the rigidity of pyridine as it impregnates the micropores. Beyond this point (i.e., $\Delta R > 62\,\Omega$), the slope of the curve abruptly decreases marking the saturation of micropore filling and a subsequent rise

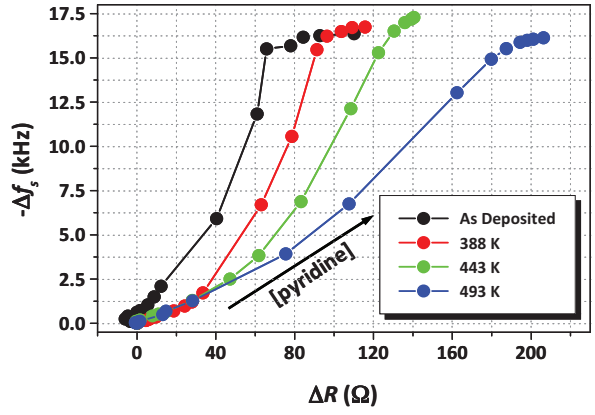

Fig. 7. Plot of frequency shifts (Δf_s) against equivalent resistance change (ΔR). Three nanoPPX coated QCM crystals were annealed at 388, 443, and 493 K prior to QCM experiments.

in the viscous loading component due to pyridine build-up on the external surface. Furthermore, as the nanoPPX annealing temperature increases, the steepness of the initial rise in the slope of the $\Delta f_s - \Delta R$ progressively decreases. This behavior indicates a diminishing Δf_s component due to rigid pyridine adsorption, which is again consistent with the decreased microporosity noted for annealed nanoPPX films in Fig. 6.

Our results are summarized by a simple micropore model, illustrated in Fig. 8, that emphasizes the role of stable or rigidly bound pyridine in the micropores. In our model, the presence of larger amorphous regions in the nanoPPX film prior to annealing allows adsorption of pyridine in large quantities into the micropores at these sites (Fig. 8, Path A). The adsorbed pyridine at these sites is stabilized by strong π–π interactions with aromatic components of the disordered parylene polymer chains comprising these amorphous regions. In contrast, annealed nanoPPX films exhibit increased crystallinity (Supplementary Information, Fig. S-4) and constricted micropores, restricting access for rigid pyridine adsorption (Fig. 8, Path B). Furthermore, pyridine adsorption in these crystalline regions is governed by weaker van der Waals interactions. As a result, this more weakly bound pyridine is readily removed during the aqueous rinsing step following pyridine adsorption, while the rigidly bound pyridine (via π–π interactions) in the micropores remains in the nanoPPX film. Consequently, the level of residual pyridine in an as-deposited nanoPPX film is higher compared to that in the annealed counterparts after the rinsing step.

Treatment of these pyridine-impregnated nanoPPX films with the Pd(II) colloid (i.e., PD1, note Section 4) results in binding of more and larger colloid particles by the as-deposited nanoPPX film due to the relatively high surface density of accessible pyridyl N-sites [26–28] on the its surface. This high density of PD1 nanoparticles is capable of initiating electroless deposition of the well developed conformal Co metal film required for efficient catalytic generation of hydrogen. On the other hand, fewer and smaller PD1 nanoparticles will be bound on nanoPPX surfaces bearing lower levels of residual pyridine [26–28]. Consequently, the Co metal films deposited onto these surfaces will be thinner and less uniform, resulting ultimately in a lower hydrogen release rate [9].

2.5. The effect of patterning on the catalytic behavior

With respect to plating time, the Co metal layer grows in a conformal manner with respect to the nanoPPX morphology, a characteristic attribute of the non-covalent metal deposition methodology [12]. At longer plating times, however, the growing metal fronts from the adjacent nanohelices merge and fuse together (note Fig. 9A), thereby reducing the active surface area for the borohydride decomposition reaction. The resultant catalytic activity of Co/nanoPPX therefore saturates at longer plating times due to decreased accessibility of the $NaBH_4$ solution to the Co surface in the interstitial regions between the nanohelices [9]. Therefore, one way to improve the reaction kinetics on the Co/nanoPPX film is using a patterned substrate instead of an unpatterned substrate for nanoPPX deposition (note Fig. 9B). Co films grown on nanoPPX deposited on a patterned substrate allow the reactants (i.e., alkaline $NaBH_4$) to better infiltrate the structure compared to Co grown on nanoPPX films deposited on an unpatterned substrate. This is reflected in the higher hydrogen release per unit area from patterned Co/nanoPPX (0.66 mL min^{-1} cm^{-2} versus 0.28 mL min^{-1} cm^{-2} for unpatterned Co/nanoPPX), as shown in Fig. 9C.

The reusability of the Co catalyst was tested by measuring the hydrogen release rate for three reaction cycles. The hydrogen release rate shows a 22.2% decrease in the catalytic activity for Co/non-patterned nanoPPX and a 15.8% decrease for Co/patterned

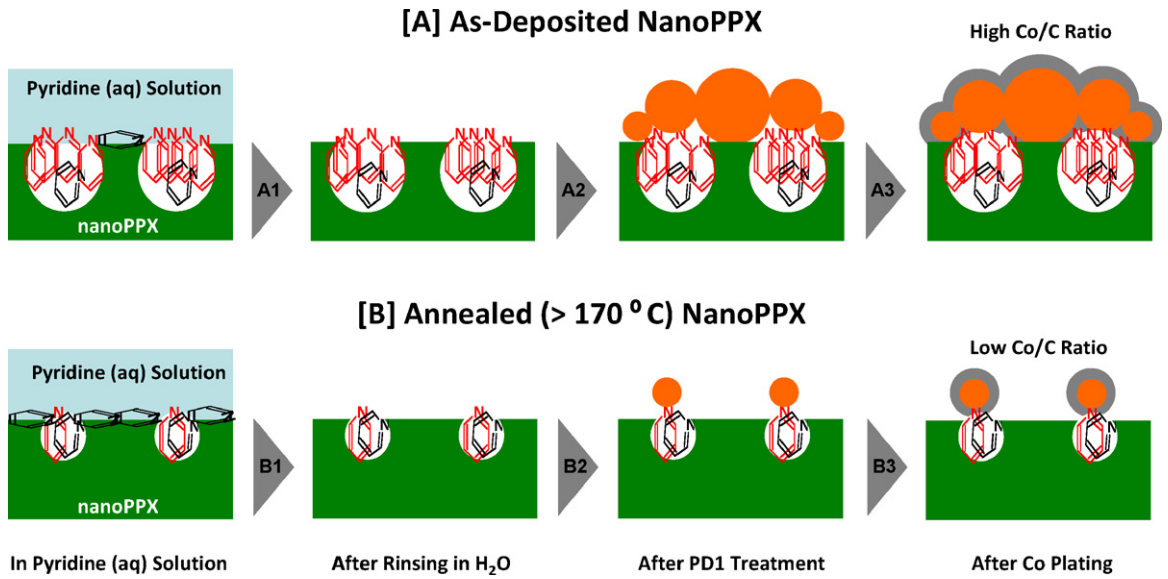

Fig. 8. Model schematic showing the effect of annealing on metal deposition rate. Green block represents crystalline domains, while the white areas denote the surface amorphous domains or micropores in the nanoPPX film that can be accessed by pyridine molecules. Paths A and B show electroless metallization via noncovalent ligand functionalization on as-deposited and annealed (at temperatures higher than 170 °C) nanoPPX films, respectively. Pyridine molecules available for PD1 binding are shown in red (N-sites at the nanoPPX surface), while those which are unavailable are shown in black (N-sites not at the nanoPPX surface or weakly bound pyridine at the nanoPPX surface). PD1 nanoparticles are shown as orange spheres and Co metal is shown in gray. (For interpretation of the references to color in this figure legend, the reader is referred to the web version of this article.)

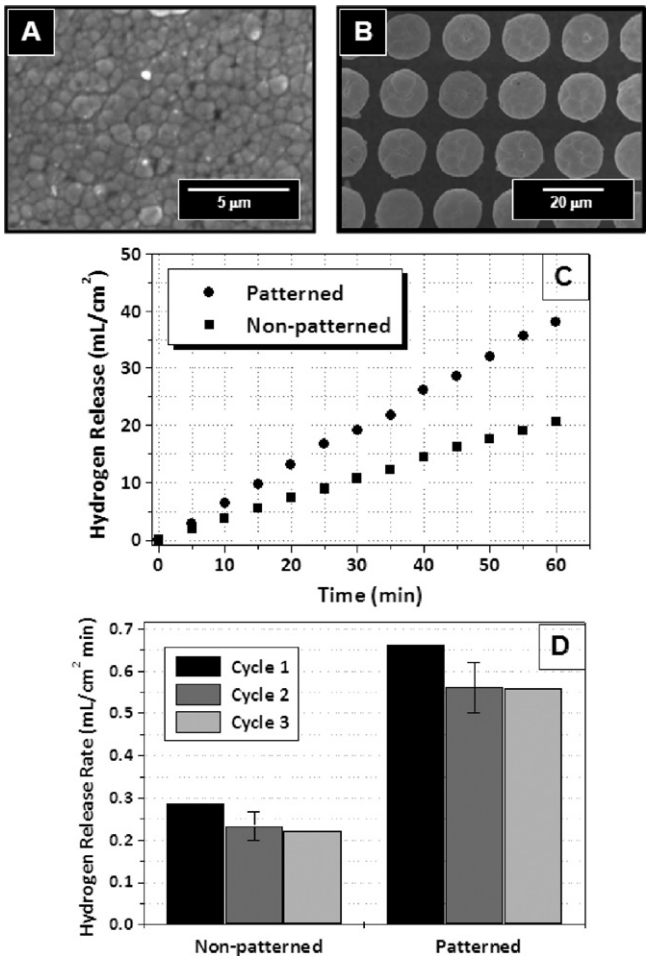

Fig. 9. (A) SEM top surface image of Co/nanoPPX. (B) SEM image of Co/patterned nanoPPX. (C) Effect of substrate patterning on hydrogen release from alkaline $NaBH_4$ solution. (D) Change of hydrogen release rate of two films (on non-patterned and patterned substrates) through three cycles.

nanoPPX after the first cycle (Fig. 9D). Thereafter, hydrogen generation activity is unchanged for each catalyst within experimental error for the remaining two cycles. Although the cause for the large initial drop in the H_2 release rates remains undetermined, loss of loosely bound metal particles and/or minor oxidation of the Co surface in the alkaline aqueous environment are likely contributors. The high stability of these catalysts is consistent with the high interfacial adhesion between the Co film and nanoPPX, which is typically observed for metal or ceramic layers grown on nanoPPX via the non-covalent functionalization method, [12,13] and therefore demonstrates its durability and reusability.

The difference in hydrogen release rates of the patterned and unpatterned films shown in Fig. 9C is consistent with expectations derived from the Hadamard–Rybczynski (HR) equation, which describes the terminal velocity, V_t, of slowly moving spherical bubbles through ambient fluid. The HR equation is given by

$$V_t = \frac{2}{3} r^2 g(\rho_b - \rho_o)\mu^* \quad (6)$$

where r is the radius of the bubble, g is the gravity, ρ_b is the density of the bubble, ρ_o is the density of the sodium borohydride solution, and μ^* is the viscosity ratio. According to the HR equation, the terminal velocity scales with the square of bubble radius. For the unpatterned substrate the H_2 bubble size is limited by the mesopore size of the nanoPPX, which corresponds to the spacing between the *metallized* nanohelices (i.e., <100 nm; note Fig. 3). For the patterned substrate, H_2 bubbles can originate in the mesopores within a cluster of nanohelices as well at the edges of the nanohelix pattern. Maximum dimensions for bubbles formed along the pattern edge will be defined by pattern spacings (i.e., ~10 to 20 μm; note Fig. 9B and Section 4). Therefore, both small and large bubbles can form for patterned films. Larger bubbles naturally contain more H_2 gas than their smaller counterparts, contributing to the enhanced H_2 output of the patterned films observed here. However, larger bubbles should also have a higher terminal velocity (or release rate for our experiment) compared to smaller ones according to the HR equation. Because attached H_2 bubbles block access of $NaBH_4$ to the Co surface, their rapid release is essential for enhancing catalyst turnover and, therefore, H_2 output. There-

fore, the creation of larger bubbles is also expected to enhance H_2 output via more rapid turnover of the Co metal surface during $NaBH_4$ decomposition. Together these factors qualitatively account for the enhanced H_2 release observed for the patterned substrate compared to unpatterned substrates in our $NaBH_4$ solutions.

3. Conclusions

In this work, we have demonstrated a novel and inexpensive method to prepare Co/nanoPPX catalyst, via a general non-covalent pyridine ligand functionalization route [12,29], for extraction of hydrogen from $NaBH_4$ [9]. The turnover rate for hydrogen generation on the cobalt surface is 2.86×10^{-6} and 6.74×10^{-6} mole $NaBH_4$ min^{-1} cm^{-2} on helical and patterned films, respectively. Furthermore, we have confirmed by means of gas physisorption studies that the chain disorder in a nanoPPX film is manifested by the presence of micropores of size ~1 to 2 nm where pyridine adsorption and stabilization takes place. In comparison, a planar film shows significantly lower micropore volume; this disparity in the porosity of the two films is responsible for the observed difference in pyridine uptake, leading to their contrasting metallization and catalytic behaviors.

The use of a Co metal catalyst on nanoPPX films for $NaBH_4$ decomposition allows significant cost reductions compared to expensive noble-metal catalysts without significantly compromising the hydrogen discharge kinetics. Cost reduction is possible not only by replacing the noble metal (e.g., Pt, Ru, etc.) by Co, but also by the scale-up capability of the entire fabrication process (i.e., OAP followed by electroless metallization). Our highest hydrogen release rate (0.66 mL min^{-1} cm^{-2}) is obtained on Co membranes deposited on nanoPPX films grown on patterned silicon substrates. However, because our nanoPPX patterns have not yet been fully optimized, even higher H_2 generation rates may be possible through further control of factors such as the pattern dimensions, Co plating efficiencies, and nanohelix shapes and dimensions.

4. Experimental

4.1. Film deposition

Planar and nanoPPX films of 5–10 μm thickness were deposited on either Si wafer or glass substrates per the procedure detailed in our previous work [10,30–34]. Briefly, a 3.64 g portion of the precursor dimer, i.e., dichloro-[2,2]-paracyclophane (PDS Inc., TX), was used to deposit planar parylene films using a Labcoater 2 deposition unit (SCS Inc., Indianapolis, IN). For a nanoPPX film, 0.3 g portion of the precursor was used and the monomeric radical flux was directed at a 10° angle to the substrate by means of a nozzle. The substrates were axially rotated (ω = 5 rpm) using a computer-controlled stepper motor during nanoPPX deposition. After deposition, the films were delaminated from the substrate and outgassed in the vacuum degas port of the analyzer for ~4 h at 298 K before initiating the gas physisorption study.

4.2. Characterization

A Micrometrics ASAP 2020 fully automated volumetric adsorption analyzer was used for N_2 and CO_2 adsorption studies on planar and nanoPPX films. QCM experiments were conducted using Maxtek RQCM (Inficon Inc., NY) controller, which allows simultaneous resonance frequency (f_s) and resistance (R) monitoring. Pristine quartz crystals coated with Cr/Au electrodes (5 MHz resonance) were purchased from SRS Inc., CA. A layer of octadecanethiol (C18-thiol) self-assembled monolayer (SAM) [35] was grown on the gold electrode before depositing the PPX film onto it. Pyridine adsorption isotherms were measured for planar and nanoPPX films in vapor phase or aqueous solution phase conditions at 298 K. ACS reagent grade pyridine from Aldrich Chemical Co. was used for all experiments. For vapor phase adsorption measurements, a PPX-coated QCM crystal coated with nanoPPX or planar film was horizontally suspended above an aqueous pyridine solution in a tightly sealed vial. During aqueous solution adsorption measurements, the PPX-coated QCM crystal was completely immersed in the solution. The entire assembly was kept in a vibration/acoustic-free isolation chamber. Pyridine was incrementally dosed in the vial to increase the concentration step-wise from 0 M to 1.5 M. The frequency and resistance were allowed to stabilize for at least 2 h before the addition of each subsequent dose. The corresponding stabilized frequency (f_s) and resistance (R) at each dosing step were recorded to obtain the adsorption isotherm and $\Delta f_s - \Delta R$ plot.

4.3. Metallization

Deionized water (18.1 MΩ cm) from a Barnstead Nanopure Diamond™ dispenser was used for all experiments. All materials were ACS reagent or equivalent and were used as received. Five nanoPPX samples were deposited on allyl-functionalized Si wafers according to the literature method [10]. Annealing of four as-deposited nanoPPX films was carried out in N_2 atmosphere at temperatures 115, 140, 170 and 220 °C on a hot plate for 1 h. Subsequent metallization was carried out using the procedure detailed in our previous publication [9]. Briefly, samples were treated with 1 M pyridine (aq) for ~48 h and rinsed in water for 4 min. The samples were then immersed in a Pd^{II}-based colloidal dispersion (designated as PD1 [36]) for 45 min. Samples were then rinsed in water for 1 min followed by plating in Co bath, prepared using procedure described in Malvadkar et al. [9], for either 1 min or 60 min. All treatment steps were timed precisely using a digital stop-watch. After Co plating, the samples were rinsed in water, dried in a filtered N_2 gas stream, and stored in a vacuum desiccator until required for hydrogen release experiments. Metallization was also carried out on nanoPPX films deposited on patterned silicon substrates. Patterned silicon substrates were prepared via photolithography to produce a square array of cylindrical pillars with 10 μm diameter and 20 μm spacing (center-to-center) between adjacent pillars and an average height of 30 μm.

4.4. Hydrogen release

We used the experimental setup described in our previous publication [9] to measure the hydrogen release rate. Briefly, $NaBH_4$ (J.T. Baker) solution in water was prepared using 2.5 wt.% $NaBH_4$ (0.677 M) and 1 wt.% NaOH (aq) solution (0.261 M) [9]. The NaOH prevents $NaBH_4$ from reacting with water directly, as the pH measured exceeded 12 at all times. The experiments for hydrogen generation from Co films were run for 1 h at room temperature. The hydrogen was collected via gas displacement of the water in a water-filled volumetric glass tube. The reusability of the Co/unpatterned nanoPPX and Co/patterned nanoPPX catalysts (preparation conditions for both catalysts: pyridine (aq) adsorption time = 48 h; PD1 treatment time = 45 min; Co plating time = 60 min) was tested under identical experimental conditions (i.e., 2.5% $NaBH_4$ and 1% NaOH) for three cycles of 1 h each. The catalysts were washed with water and dried with N_2 gas after each cycle and stored in a vacuum desiccator for 24 h before use for the next cycle.

Acknowledgements

The authors gratefully acknowledge financial support for this work from the Pennsylvania State University, Wyss Institute for Biologically Inspired Engineering at Harvard, and the Office of Naval Research under the Naval Research Laboratory Core 6.1 Research Program. The authors thank Prof. Aman Haque (Penn State) for providing the patterned substrates.

Appendix A. Supplementary data

Supplementary data associated with this article can be found, in the online version, at doi:10.1016/j.jpowsour.2011.05.071.

References

[1] K.C. Hoffman, J.J. Reilly, F.J. Salzano, C.H. Waide, R.H. Wiswall, W.E. Winsche, International Journal of Hydrogen Energy 1 (1976) 133–151.
[2] L. Schlapbach, A. Zuttel, Nature 414 (2001) 353–358.
[3] Y. Kojima, K. Suzuki, K. Fukumoto, M. Sasaki, T. Yamamoto, Y. Kawai, H. Hayashi, International Journal of Hydrogen Energy 27 (2002) 1029–1034.
[4] P. Krishnan, T.H. Yang, W.Y. Lee, C.S. Kim, Journal of Power Sources 143 (2005) 17–23.
[5] S.C. Amendola, S.L. Sharp-Goldman, M.S. Janjua, M.T. Kelly, P.J. Petillo, M. Binder, Journal of Power Sources 85 (2000) 186–189.
[6] C. Cakanyildirim, M. Guru, International Journal of Hydrogen Energy 33 (2008) 4634–4639.
[7] Y. Kojima, T. Haga, International Journal of Hydrogen Energy 28 (2003) 989–993.
[8] E.H. Park, S.U. Jeong, U.H. Jung, S.H. Kim, J. Lee, S.W. Nam, T.H. Lim, Y.J. Park, Y.H. Yu, International Journal of Hydrogen Energy 32 (2007) 2982–2987.
[9] N. Malvadkar, S. Park, M. Urquidi-MacDonald, H. Wang, M.C. Demirel, Journal of Power Sources 182 (2008) 323–328.
[10] M. Cetinkaya, N. Malvadkar, M.C. Demirel, Journal of Polymer Science Part B: Polymer Physics 46 (2008) 640–648.
[11] S.C. Amendola, S.L. Sharp-Goldman, M.S. Janjua, N.C. Spencer, M.T. Kelly, P.J. Petillo, M. Binder, International Journal of Hydrogen Energy 25 (2000) 969–975.
[12] M.C. Demirel, M. Cetinkaya, A. Singh, W.J. Dressick, Advanced Materials 19 (2007) 4495–4499.
[13] N. Malvadkar, W.J. Dressick, M.C. Demirel, Journal of Materials Chemistry 19 (2009) 4796–4804.
[14] G. Sauerbrey, Zeitschrift Fur Physik 155 (1959) 206–222.
[15] S. Brunauer, P.H. Emmett, E. Teller, Journal of the American Chemical Society 60 (1938) 309–319.
[16] S.Z. Qiao, S.K. Bhatia, X.S. Zhao, Microporous and Mesoporous Materials 65 (2003) 287–298.
[17] E.P. Barrett, L.G. Joyner, P.P. Halenda, Journal of the American Chemical Society 73 (1951) 373–380.
[18] N.A. Malvadkar, M.J. Hancock, K. Sekeroglu, W.J. Dressick, M.C. Demirel, Nature Materials 9 (2010) 1023–1028.
[19] S. Boduroglu, M. Cetinkaya, W.J. Dressick, A. Singh, M.C. Demirel, Langmuir 23 (2007) 11391–11395.
[20] N.A. Malvadkar, G. Demirel, M. Poss, A. Javed, W.J. Dressick, M.C. Demirel, Journal of Physical Chemistry C 114 (2010) 10730–10738.
[21] N.A. Malvadkar, K. Sekeroglu, W.J. Dressick, M.C. Demirel, Langmuir 26 (2010) 4382–4391.
[22] M.M. Dubinin, V.A. Astakhov, Advances in Chemical Series 102 (1971) 69–75.
[23] H.F. Stoeckli, Journal of Colloid and Interface Science 59 (1977) 184–185.
[24] S.J. Martin, V.E. Granstaff, G.C. Frye, Analytical Chemistry 63 (1991) 2272–2281.
[25] S. Storck, H. Bretinger, W.F. Maier, Applied Catalysis A 174 (1998) 137–146.
[26] S.L. Brandow, W.J. Dressick, C.R.K. Marrian, G.-M. Chow, J.M. Calvert, Journal of the Electrochemical Society 142 (1995) 2233–2243.
[27] R.R. Price, W.J. Dressick, A. Singh, Journal of the American Chemical Society 125 (2003) 11259–11263.
[28] D. Zabetakis, W.J. Dressick, ACS Applied Materials & Interfaces 1 (2009) 4–25.
[29] M.-S. Chen, S.L. Brandow, T.L. Schull, D.B. Chrisey, W.J. Dressick, Advanced Functional Materials 15 (2005) 1364–1375.
[30] M. Cetinkaya, S. Boduroglu, M.C. Demirel, Polymer 48 (2007) 4130–4134.
[31] M. Cetinkaya, M.C. Demirel, Chemical Vapor Deposition 15 (2009) 101–105.
[32] M.C. Demirel, Colloids and Surfaces A: Physicochemical and Engineering Aspects 321 (2008) 121–124.
[33] M.C. Demirel, S. Boduroglu, M. Cetinkaya, A. Lakhtakia, Langmuir 23 (2007) 5861–5863.
[34] E. So, M.C. Demirel, K.J. Wahl, Journal of Physics D: Applied Physics 43 (2010) 045403.
[35] T. Ishida, M. Hara, I. Kojima, S. Tsuneda, N. Nishida, H. Sasabe, W. Knoll, Langmuir 14 (1998) 2092–2096.
[36] W.J. Dressick, L.M. Kondracki, M.S. Chen, S.L. Brandow, E. Matijević, J.M. Calvert, Colloids and Surfaces A: Physicochemical and Engineering Aspects 108 (1996) 101–111.